

1 Revision 1

2

Word count: 9327

3 **Single-Crystal Elasticity of (Al,Fe)-bearing Bridgmanite up to 82 GPa**

4 Suyu Fu^{a,1,*}, Yanyao Zhang^a, Takuo Okuchi^{b,2}, Jung-Fu Lin^{a,*}

5 ^aDepartment of Geological Sciences, Jackson School of Geosciences, The University of Texas at
6 Austin, Austin, TX, USA

7 ^bInstitute for Planetary Materials, Okayama University, Misasa, Japan

8 ¹Now at School of Earth and Space Exploration, Arizona State University, Tempe, Arizona, USA.

9 ²Now at Institute for Integrated Radiation and Nuclear Science, Kyoto University, Kyoto, Japan.

10 *Corresponding author: Jung-Fu Lin (afu@jsg.utexas.edu), Suyu Fu (fsyxhy@gmail.com)

11

12

ABSTRACT

13 Thermoelastic properties of mantle candidate minerals are essential to our understanding of
14 geophysical phenomena, geochemistry, and geodynamic evolutions of the silicate Earth.
15 However, the lower-mantle mineralogy remains much debated due to the lack of single-crystal
16 elastic moduli (C_{ij}) and aggregate sound velocities of (Al,Fe)-bearing bridgmanite, the most
17 abundant mineral of the planet, at the mid-lower mantle pressure-temperature (P-T) conditions.
18 Here we report single-crystal C_{ij} of (Al,Fe)-bearing bridgmanite, $\text{Mg}_{0.88}\text{Fe}_{0.1}\text{Al}_{0.14}\text{Si}_{0.90}\text{O}_3$ (Fe10-
19 Al14-Bgm) with $\text{Fe}^{3+}/\sum\text{Fe} \approx 0.65$, up to ~ 82 GPa using X-ray diffraction (XRD), Brillouin light
20 scattering (BLS), and impulsive stimulated light scattering (ISLS) measurements in diamond

21 anvil cells (DACs). Two crystal platelets with orientations of (-0.50, 0.05, -0.86) and (0.65, -0.59,
22 0.48), that are sensitive to deriving all nine C_{ij} , are used for compressional and shear wave
23 velocity (V_P and V_S) measurements as a function of azimuthal angles over 200° at each
24 experimental pressure. Our results show that all C_{ij} of single-crystal Fe10-Al14-Bgm increase
25 monotonically with pressure with small uncertainties of 1-2% ($\pm 1\sigma$), except C_{55} and C_{23} , which
26 have uncertainties of 3-4%. Using the third-order Eulerian finite-strain equations to model the
27 elasticity data yields the aggregate adiabatic bulk and shear moduli and respective pressure
28 derivatives at the reference pressure of 25 GPa: $K_S = 326 (\pm 4) \text{ GPa}$, $\mu = 211 (\pm 2) \text{ GPa}$, and
29 $K'_S = 3.32 (\pm 0.04) \text{ GPa}$, $\mu' = 1.66 (\pm 0.02)$. The high-pressure aggregate V_S and V_P of Fe10-
30 Al14-Bgm are 2.6-3.5% and 3.1-4.7% lower than those of MgSiO_3 bridgmanite end member,
31 respectively. These data are used with literature reports on bridgmanite with different Fe and Al
32 contents to quantitatively evaluate pressure and compositional effects on their elastic properties.
33 Comparing with one-dimensional seismic profiles, our modeled velocity profiles of lower-mantle
34 mineral assemblages at relevant P-T suggest that the lower mantle could likely consist of (Al,Fe)-
35 bearing bridgmanite, about 89 vol%. After taking into account uncertainties, it is still
36 indistinguishable from pyrolitic or chondritic models.

37 **Keywords (<6 keywords):** single-crystal elasticity, bridgmanite, lower mantle, pyrolite,
38 chondrite

39

40

INTRODUCTION

41 Earth's lower mantle, the most voluminous region of the planet, plays a key role in regulating
42 physical, chemical, and dynamic interactions between the core and upper mantle as well as the crust.

43 Geochemical and petrological observations indicate that the upper mantle likely consists of pyrolite
44 with approximately three portions of peridotite and one portion of basalt (Ringwood, 1975). If one
45 assumes the whole mantle is chemically homogenous in major elements, a pyrolitic lower mantle
46 would have ~75 vol% (Al,Fe)-bearing bridgmanite [(Mg,Fe,Al),(Fe,Al,Si)O₃, Bgm], ~18 vol%
47 ferropericlase [(Mg,Fe)O, Fp], and ~7 vol% CaSiO₃ davemaoite (Irifune et al., 2010; Tschauner et
48 al., 2021). However, such a pyrolitic model with Mg/Si~1.25 has much less Si than the chondritic
49 bulk Earth model with Mg/Si~1.0 from cosmochemical constraints (McDonough and Sun, 1995).
50 To address the “missing Si” conundrum in the silicate Earth, Si as a light element in the core
51 (Allègre et al., 1995) and/or a Si-rich lower mantle (Hofmann, 1997) have been proposed
52 previously. Moreover, some recent studies suggest that comparisons of velocity and density profiles
53 between seismic observations (Dziewonski and Anderson, 1981; Kennett et al., 1995) and mineral
54 physics models (Irifune et al., 2010; Kurnosov et al., 2017; Mashino et al., 2020; Murakami et al.,
55 2012) could provide important insights into the lower-mantle mineralogy. This would require a
56 complete and reliable elasticity dataset of the lower-mantle candidate minerals with small
57 uncertainties.

58 Bridgmanite is suggested to be the most abundant lower-mantle mineral (Ringwood, 1975).
59 Despite extensive theoretical studies on its elasticity at high P-T (Karki et al., 1997; Shukla and
60 Wentzcovitch, 2016; Wentzcovitch et al., 2004), experimental investigations on this subject are still
61 rather limited to polycrystalline samples or single crystals at relatively low pressures. In addition, as
62 much as 10 mol% Fe³⁺ and Al³⁺ could substitute the dodecahedral-site (A-site) Mg²⁺ and
63 octahedral-site (B-site) Si⁴⁺ in the crystal structure of bridgmanite via charge-coupled substitution
64 (e.g., Frost et al., 2004; McCammon, 1997), whose effects on the elastic properties also need
65 investigation. Of particular examples are the reports by Murakami et al. (2012) and Mashino et al.

66 (2020) that measured V_S of polycrystalline Al- and/or Fe-bearing bridgmanite up to 124 GPa using
67 BLS technique to suggest a perovskitic lower mantle with greater than 92 vol% bridgmanite. A
68 recent study measured both V_P and V_S of polycrystalline Fe-bearing bridgmanite,
69 $\text{Mg}_{0.96}\text{Fe}^{2+}_{0.036}\text{Fe}^{3+}_{0.014}\text{Si}_{0.99}\text{O}_3$, up to 70 GPa at 300 K using both ISLS and BLS methods and
70 observed a drastic softening in V_P at 42.6-58 GPa and a slight increase in V_S above 40 GPa (Fu et al.,
71 2018). This finding has been attributed to the spin transition of B-site Fe^{3+} in bridgmanite (Fu et al.,
72 2018; Shukla et al., 2016). However, the sound velocity data from polycrystalline samples in DACs
73 to represent their bulk properties has been questioned in Earth science because of issues with
74 velocity anisotropies, textures, and direction-dependent acoustic phonon intensities (Speziale et al.,
75 2014).

76 As to single-crystal elasticity study, Criniti et al. (2021) and Kurnosov et al. (2017) measured
77 velocities in BLS experiments to determine single-crystal elasticity of MgSiO_3 and (Al,Fe)-bearing
78 bridgmanite, $\text{Mg}_{0.9}\text{Fe}_{0.1}\text{Al}_{0.1}\text{Si}_{0.9}\text{O}_3$ (Fe10-Al10-Bgm), up to 79 and 40 GPa, respectively. Due to
79 the technical limitation in BLS measurements where V_P peaks of bridgmanite can be blocked by
80 diamond V_S signals above 20 GPa, these studies (Criniti et al., 2021; Kurnosov et al., 2017) used a
81 global fit scheme by fitting all the velocity data together to derive single-crystal C_{ij} at high pressure.
82 It has been debated whether such a global fit scheme is appropriate because that those greater
83 uncertainties of derived C_{ij} at higher pressures were compensated by higher quality data at lower
84 pressures (Kurnosov et al., 2018; Lin et al., 2018). To improve the full elasticity data, a recent study
85 determined single-crystal elasticity of (Al,Fe)-bearing bridgmanite with two compositions,
86 $\text{Mg}_{0.95}\text{Fe}^{2+}_{0.033}\text{Fe}^{3+}_{0.027}\text{Al}_{0.04}\text{Si}_{0.96}\text{O}_3$ (Fe6-Al4-Bgm) and $\text{Mg}_{0.89}\text{Fe}^{2+}_{0.024}\text{Fe}^{3+}_{0.096}\text{Al}_{0.11}\text{Si}_{0.89}\text{O}_3$ (Fe12-
87 Al11-Bgm), by individually fitting velocity data from both ISLS and BLS measurements at each
88 experimental pressure of 25 and 35 GPa (Fu et al., 2019b). The results showed that the coupled

89 substitution of Fe and Al in bridgmanite significantly decreases its V_P and V_S . In a nutshell, because
90 of the lack of single-crystal elasticity data of (Al,Fe)-bearing bridgmanite across the whole lower-
91 mantle pressure, it has been a great challenge for a better understanding of the lower-mantle
92 composition and seismic observations.

93 Here, we reported single-crystal C_{ij} of (Al,Fe)-bearing bridgmanite, $\text{Mg}_{0.88}\text{Fe}_{0.1}\text{Al}_{0.14}\text{Si}_{0.90}\text{O}_3$
94 (Fe10-Al14-Bgm) with $\text{Fe}^{3+}/\sum\text{Fe} \sim 0.65$, up to ~ 82 GPa at 300 K using V_P data from ISLS, V_S data
95 from BLS, and pressure-density relationship (equation of state, EoS) from synchrotron XRD
96 measurements in DACs. Two platelets with crystallographic orientations of (-0.50, 0.05, -0.86) and
97 (0.65, -0.59, 0.48) are selected with sufficient sensitivities to derive full C_{ij} with small uncertainties
98 (Figure 1). The use of ISLS and BLS techniques (Fu et al., 2018; Yang et al., 2015) enables both V_P
99 and V_S measurements on selected platelets as a function of azimuthal angles at high pressure
100 (Figures 2 and S1 and Table S1), that overcomes previous difficulties when only using BLS
101 technique (Criniti et al., 2021; Kurnosov et al., 2017; Mashino et al., 2020; Murakami et al., 2012).
102 Together with literature reports on elastic properties of bridgmanite with different Al and Fe
103 contents, we can quantitatively evaluate the effect of Fe and Al on its adiabatic bulk and shear
104 moduli (K_S and μ) at high pressure. Our results are used in a self-consistent thermoelastic model to
105 evaluate velocity profiles of lower-mantle mineral aggregates at relevant P-T, and then applied to
106 help us better constrain the lower-mantle composition.

107 **EXPERIMENTAL METHODS**

108 Single-crystal bridgmanite with run number 5K2667 was synthesized using the 5000-ton
109 Kawai-type multi-anvil apparatus at the Institute for Planetary Materials at Okayama University.
110 Starting materials of magnesium hydroxide $[\text{Mg}(\text{OH})_2]$, enstatite $[\text{MgSiO}_3]$, aluminum oxide
111 $[\text{Al}_2\text{O}_3]$, and iron oxide $[\text{}^{57}\text{FeO}]$ were mechanically mixed with desired weight percentages, and

112 were then sealed into a Pt capsule. The Pt capsule in the sample assemblage was compressed and
113 heated up to ~24 GPa and ~1800 °C for 20 h to synthesize single-crystal (Al,Fe)-bearing
114 bridgmanite. Details of sample synthesis and characterizations on its chemistry, $\text{Fe}^{3+}/\Sigma\text{Fe}$, and
115 crystallinity have been well documented in a previous study (Fu et al., 2019a). Results from
116 electron microprobe analysis, Mössbauer spectroscopy, Raman spectroscopy, transmission electron
117 microscopy, and synchrotron XRD reveal that the synthesized bridgmanite is chemically
118 homogeneous and inclusions-free in micrometer- to nanometer-spatial resolutions with a
119 composition of $\text{Mg}_{0.88}\text{Fe}_{0.1}\text{Al}_{0.14}\text{Si}_{0.90}\text{O}_3$ and $\text{Fe}^{3+}/\Sigma\text{Fe} \sim 0.65$. Single-crystal XRD results show
120 sharp diffraction spots with lattice parameters of $a = 4.7875(3) \text{ \AA}$, $b = 4.9423(2) \text{ \AA}$, $c = 6.9205(6)$ at
121 ambient conditions, confirming the high quality of single-crystal samples needed for elasticity
122 measurements.

123 Bridgmanite has an orthorhombic structure (*Pbnm*) in lower-mantle P-T with nine independent
124 C_{ij} to be constrained. Following a literature procedure (Fu et al., 2019b), we first selected and
125 double-sided polished several platelets to ~25-30 μm thick using 3M diamond films for synchrotron
126 single-crystal XRD measurements at ambient conditions at 13ID-D GeoSoilEnviroCARS
127 (GSECARS) of the Advanced Photon Source (APS), Argonne National Laboratory (ANL). An
128 incident X-ray with a 0.3344- Å wavelength was used for the measurements in which $\pm 15^\circ$ rotations
129 of each platelet about the vertical axis of the sample stage were employed to determine its
130 crystallographic orientation with an uncertainty of $< 0.2^\circ$. Then, the determined orientation of each
131 platelet was used to calculate its sensitivity of synthetic velocities to C_{ij} so that we can select
132 appropriate platelets for velocity measurements and derivations of full C_{ij} with small uncertainties.
133 Based on these analyses (Figure 1), two platelets with orientations of (-0.50, 0.05, -0.86) and (0.65,
134 -0.59, 0.48) with sufficient sensitivities were used for velocity measurements.

135 BLS and ISLS measurements were conducted on the selected platelets loaded into DACs up to
136 82 GPa with a pressure interval of 6-10 GPa in the Mineral Physics Laboratory of the Department
137 of Geological Sciences at The University of Texas at Austin. Re gaskets with initial thicknesses of
138 250 μm were pre-indented to 25 GPa or $\sim 28\text{-}\mu\text{m}$ thick using short symmetric 200- μm -culet DACs.
139 Pre-indented areas were drilled with 130- μm diameter holes as sample chambers. Selected platelets
140 were cut using focused ion beam into circular shapes (Marquardt and Marquardt, 2012), $\sim 60\text{-}70\ \mu\text{m}$
141 in diameter, and were polished down to 10- μm thick to be loaded into sample chambers in two runs.
142 Neon was used as pressure medium and a ruby sphere pressure calibrant was placed close to the
143 sample to minimize pressure uncertainties (Figure 2c insert). We note that, to achieve pressure
144 stability and ensure pressure consistency between two runs, each DAC was kept at the target
145 experimental pressure for 2-3 days before velocity measurements. Ruby fluorescence was taken
146 before and after each measurement to evaluate pressure uncertainties (Dewaele et al., 2004). We
147 used the ruby pressure scale by Dewaele et al. (2004) because of its internal consistency with the
148 Au pressure scale used in our complementary XRD experiments. We also note that synchrotron
149 single-crystal XRD of the loaded platelets in DACs were conducted at several high-pressure points
150 at 13 ID-D of GSECARS at APS, ANL. The circular and round diffraction peaks with average
151 FWHM of $\sim 0.04^\circ\text{-}0.07^\circ$ confirmed the high-quality of our crystals up to 76 GPa in neon medium
152 (Figure 2a-b). Analyses of XRD show consistent orientation information with small deviations ($<1^\circ$)
153 as determined at ambient conditions.

154 The BLS system is equipped with a solid-state green laser of 532-nm wavelength and a $\sim 30\text{-}\mu\text{m}$
155 focused beam size (Coherent Verdi V2), a JRS six-pass tandem Fabry-Perot Interferometer, and an
156 APD detector (Laser Components Count-10B). We collected BLS spectra at a forward scattering
157 geometry with an external scattering angle of 48.1° . The ISLS system uses a pump-and-probe

158 technique with an infrared pump laser of 1064-nm wavelength and a green probe laser of 532-nm
159 wavelength. Both lasers have pulse widths of 15 ps and repetition rates of 200,000 Hz. Two
160 excitation beams, that are split from the pump laser, are recombined at the sample position with a
161 crossing angle of 20.3°. The focused probe laser on the sample has a beam size of 30-40 μm . To
162 avoid potential geometrical errors, both BLS and ISLS systems were aligned precisely using a
163 series of reference spots and iris diaphragms, and were calibrated using distilled water and standard
164 glass (Fu et al., 2018). To avoid potential sample degradation due to the metastability of
165 bridgmanite at low pressures, we intentionally started BLS and ISLS measurements from ~ 24 GPa
166 where bridgmanite is expected to be thermodynamically stable. BLS and ISLS spectra were
167 collected on two loaded samples as a function of azimuthal angles over 200° with a 10° -step
168 rotation at each experimental pressure (Table S1). Collected BLS spectra were used to derive V_S
169 and time-domain ISLS spectra were Fourier-transformed into frequency-domain power spectra to
170 derive V_P of the sample at high pressure (Figure 2c-e).

171 A complimentary XRD run was conducted on single-crystal Fe10-Al14-Bgm up to 75 GPa at
172 300 K to evaluate its pressure-volume relationship at 13 ID-D of GSECARS at APS, ANL (Figure
173 S1 and Table S2). Here, we followed a literature experimental procedure (Fu et al., 2018) by
174 loading a piece of Fe10-Al14-Bgm platelet, ~ 20 μm in length and ~ 8 μm in thickness, into a
175 symmetric DAC with 200- μm culets, together with Au as the pressure calibrant and neon as the
176 pressure medium. These results allow us to calculate the high-pressure density (ρ) of the crystal,
177 that is needed for deriving the full C_{ij} .

178

179

RESULTS AND DISCUSSION

180

Single-crystal elasticity of Fe10-Al14-Bgm at high pressure

181

The measured BLS and ISLS spectra display high signal-to-noise ratios and are used to derive

182

V_{S1} , V_{S2} , and V_P of single-crystal Fe10-Al14-Bgm up to ~82 GPa (Figure 2c-e). We used

183

Christoffel's equations (Every, 1980) to fit the obtained velocities as a function of azimuthal angles

184

over a range of 200° and derived the full C_{ij} of single-crystal Fe10-Al14-Bgm at each experimental

185

pressure (Figure 3):

$$|C_{ijkl}n_i n_j - \rho v^2 \delta_{ik}| = 0 \quad (1)$$

186

where C_{ijkl} is the elastic tensor with full suffix notation, which is contracted to C_{ij} in Voigt form in

187

this study, v are measured velocities of V_P , V_{S1} , and V_{S2} , n_i are wave vector direction cosines, and δ_{ik}

188

is the Kronecker delta. Results show that all C_{ij} values increase monotonically with pressure up to

189

82 GPa with uncertainties ($\pm 1\sigma$) of 1-2%, except C_{55} and C_{23} with errors of ~3-4%, which are

190

consistent with our sensitivity test (Figure 4 and Table 1). We note that only BLS measurements

191

were conducted on the platelet of (0.65, -0.59, 0.48) with sufficient V_{S1} and V_{S2} information to

192

shorten experimental time and decrease the risk of breaking diamonds. Overall, the use of combined

193

BLS and ISLS measurements on two sensitive crystal platelets with extended V_S and V_P datapoints

194

at high pressure assures derivations of all C_{ij} with acceptable uncertainties.

195

Comparison of the obtained C_{ij} of Fe10-Al14-Bgm with literature studies shows that almost all

196

C_{ij} values except C_{12} have similar pressure dependences to those from theoretical calculations on

197

MgSiO₃ bridgmanite (Karki et al., 1997; Li et al., 2005; Wentzcovitch et al., 2004) and those from

198

experimental investigations on MgSiO₃ bridgmanite (Criniti et al., 2021) and Fe10-Al10-Bgm

199 (Kurnosov et al., 2017). Compared to MgSiO_3 bridgmanite end member (Criniti et al., 2021), C_{11} ,
200 C_{22} , C_{33} , and C_{44} of Fe10-Al14-Bgm are about 8%, 7%, 6%, 12% lower, respectively, C_{66} and C_{23}
201 of Fe10-Al14-Bgm displays 10-15% increase, and C_{55} and C_{13} of Fe10-Al14-Bgm show weak
202 changes. We also found that the shear moduli of Fe10-Al14-Bgm show $C_{66} > C_{44}$, which is opposite
203 from the MgSiO_3 bridgmanite with $C_{44} > C_{66}$. Early studies have shown that the Fe and Al
204 substitution in bridgmanite can greatly affects its C_{ij} , especially on longitudinal and shear moduli
205 (Fu et al., 2019b; Li et al., 2005). Therefore, we attribute the aforementioned differences to the Fe
206 and Al compositional effect. As to the C_{12} , our Fe10-Al14-Bgm has much lower values than
207 theoretical and experimental reports on MgSiO_3 bridgmanite at pressures above 40 GPa (Criniti et
208 al., 2021; Karki et al., 1997; Li et al., 2005; Wentzcovitch et al., 2004). It should be noted that the
209 C_{12} of Fe10-Al14-Bgm is comparable to that of Fe10-Al10-Bgm within the overlapped
210 experimental pressure range when using the individual fit scheme (Lin et al., 2018) instead of the
211 global fit (Kurnosov et al., 2017). Criniti et al. (2021) used a global fit scheme to derive the single-
212 crystal C_{ij} of MgSiO_3 bridgmanite up to 79 GPa but they can only report reliable C_{ij} below 30 GPa
213 using the individual fit scheme. This is because the individual fit scheme does not work on their
214 velocity data with limited V_P information at pressures above 50 GPa (Criniti et al., 2021). As
215 discussed by Lin et al. (2018), the global fit approach, that takes all the velocity data at high
216 pressure to derive C_{ij} values, would lead to the compensation of C_{ij} errors at higher pressure by the
217 lower pressure data that have lower uncertainties. As demonstrated in our analyses (Figures 1 and
218 3), extensive V_P and V_S datapoints at each experimental pressure are key to deriving C_{ij} values with
219 small uncertainties. Thermoelastic modelling of the C_{ij} values taken from the literature should thus
220 be exercised with caution in error propagations.

221 To quantitatively derive pressure derivatives of all C_{ij} , we used a finite-strain theory (Stixrude
222 and Lithgow-Bertelloni, 2005) to fit these high-pressure results (Figure 4 and Table 2):

$$C_{ij} = (1 + 2f)^{5/2}(C_{ij0} + a_1f + a_1f^2) \quad (2)$$

$$a_1 = (3K_{S0}C'_{ij0} - 5C_{ij0}) \quad (3)$$

$$a_2 = 6K_{S0}C'_{ij} - 14C_{ij0} - 1.5K_{S0}\Delta(3K'_{S0} - 16) \quad (4)$$

223 where C'_{ij0} and K'_{S0} are pressure derivatives of single-crystal elastic moduli, C_{ij0} , and adiabatic bulk
224 modulus, K_{S0} , respectively, at the reference pressure, Δ is a constant parameter calculated as:
225 $\Delta = -\delta_{ij}\delta_{kl} - \delta_{il}\delta_{jk} - \delta_{jl}\delta_{ik}$, with values of -3 for C_{11} , C_{22} , C_{33} , and of -1 for C_{44} , C_{55} , C_{66} , C_{12} ,
226 C_{13} , C_{23} . The Eulerian strain (f) is expressed as:

$$f = \frac{1}{2} \left[(V_0/V)^{2/3} - 1 \right] \quad (5)$$

227 where V_0 is the unit cell volume at ambient conditions and V is the unit cell volume at high pressure
228 from XRD measurements (see supplementary materials). Here, we used 25 GPa, our initial
229 experimental pressure for velocity measurements, as the reference pressure for the finite-strain
230 fitting because of the thermodynamic stability of bridgmanite (the same scheme was used for K_S
231 and μ in the followings). Our fitting results show that C_{33} has a greater pressure derivative than the
232 other two principle longitudinal moduli of C_{11} and C_{22} , which leads to $C_{33} > C_{22}$ above ~70 GPa
233 (Figure 4). This is consistent with the trend of MgSiO₃ bridgmanite (Criniti et al., 2021) although
234 there are slight variations in the pressure derivatives. On the other hand, the pressure derivatives of
235 shear moduli in Fe10-Al14-Bgm exhibit $C_{44} > C_{66} > C_{55}$. With pressure increasing, the smallest
236 shear modulus at ambient, C_{44} , exceeds C_{55} above 30 GPa and is expected to be greater than C_{66} at

237 the lowermost mantle pressure. In comparison, among the shear moduli in MgSiO₃ bridgmanite, its
238 C_{66} is the smallest at ambient and has the largest pressure derivative: C_{66} is expected to higher than
239 C_{55} and C_{44} above 40 GPa and megabar pressure, respectively (Criniti et al., 2021). The off-
240 diagonal moduli of Fe10-Al14-Bgm display $C_{23} > C_{13} > C_{12}$ at all the pressure range with similar
241 trends for their pressure derivatives. In particular, our Fe10-Al14-Bgm has a 50% lower pressure
242 derivatives of C_{12} than MgSiO₃ bridgmanite (Criniti et al., 2021), which might be due to the use of a
243 global fit scheme by Criniti et al. (2021). Our results on the single-crystal C_{ij} and associated
244 pressure derivatives of Fe10-Al14-Bgm suggest that Fe and Al substitutions play a key role in the
245 elastic properties of bridgmanite. Elasticity of bridgmanite with a relevant Al and Fe composition in
246 the lower mantle is more appropriate for geophysical implications.

247 **Elastic moduli and sound velocities of bridgmanite aggregates at high pressure**

248 K_S and μ of bridgmanite aggregates can be calculated from its single-crystal C_{ij} by using a
249 Voigt-Reuss-Hill averaging scheme (Hill, 1952):

$$K_V = (C_{11} + C_{22} + C_{33} + 2(C_{12} + C_{13} + C_{23}))/9 \quad (6)$$

$$K_R = D/E \quad (7)$$

$$K_S = (K_V + K_R)/2 \quad (8)$$

$$\mu_V = (C_{11} + C_{22} + C_{33} + 3(C_{44} + C_{55} + C_{66}) - (C_{12} + C_{13} + C_{23}))/15 \quad (9)$$

$$\mu_R = 15/\left(\frac{4F}{D} + 3\left(\frac{1}{C_{44}} + \frac{1}{C_{55}} + \frac{1}{C_{66}}\right)\right) \quad (10)$$

$$\mu = (\mu_V + \mu_R)/2 \quad (11)$$

250 where K_V (μ_V) and K_R (μ_R) are upper Voigt and lower Reuss bounds of K_S (μ), respectively, and D ,
251 E , and F are three constants, calculated as:

$$D = C_{13}(C_{12}C_{23} - C_{13}C_{22}) + C_{23}(C_{12}C_{13} - C_{11}C_{23}) + C_{33}(C_{11}C_{22} - C_{12}C_{12}) \quad (12)$$

$$E = C_{11}(C_{22} + C_{33} - 2C_{23}) + C_{22}(C_{33} - 2C_{13}) - 2C_{12}C_{33} + C_{12}(2C_{23} - C_{12}) + C_{13}(2C_{12} - C_{13}) + C_{23}(2C_{13} - C_{23}) \quad (13)$$

$$F = C_{11}(C_{22} + C_{33} + C_{23}) + C_{22}(C_{33} + C_{13}) + C_{12}C_{33} - C_{12}(C_{23} + C_{12}) - C_{13}(C_{12} + C_{13}) - C_{23}(C_{13} + C_{23}) \quad (14)$$

252 Accordingly, aggregate V_P and V_S of the single-crystal Fe10-Al14-Bgm can be calculated using:

$$V_P = \sqrt{(K_S + 4\mu/3)/\rho} \quad (15)$$

$$V_S = \sqrt{\mu/\rho} \quad (16)$$

253 Standard derivations ($\pm 1\sigma$) on the elastic moduli and aggregate velocities can be calculated using
254 these equations with standard error propagations. Our results show that aggregate V_S and V_P values
255 of Fe10-Al14-Bgm increase monotonically with pressure up to ~82 GPa with uncertainties less than
256 1.0% (Figure 5). Compared with literature reports on aggregate elastic properties of polycrystalline
257 and single-crystal bridgmanite (Chantel et al., 2012; Criniti et al., 2021; Fu et al., 2019b; Jackson et
258 al., 2005; Karki et al., 1997; Kurnosov et al., 2017; Lin et al., 2018; Murakami et al., 2012), our K_S ,
259 μ , V_P , and V_S show generally consistent profiles for the first order and display strong Fe and Al
260 effect: V_S and V_P of Fe10-Al14-Bgm are 2.6% and 3.1% lower than those of MgSiO₃ bridgmanite
261 (Criniti et al., 2021), respectively, at 25 GPa and the values increase up to 3.5% and 4.7% for V_S
262 and V_P , respectively, at 80 GPa. This indicates an increasing Fe and Al effect on sound velocities of

263 bridgmanite with pressure. We also notice that the sound velocities of Fe10-Al14-Bgm are
264 comparable to those of Fe10-Al10-Bgm by Kurnosov et al. (2017) within the overlapped
265 experimental pressures of 25-40 GPa due to their similar Fe and Al contents. On the other hand,
266 literature studies suggest that B-site Fe³⁺ in Fe-bearing bridgmanite could undergo a spin transition
267 at approximately 40-60 GPa and cause an abrupt V_P softening (Fu et al., 2018). The monotonical
268 increase of V_S and V_P in our Fe10-Al14-Bgm with pressure up to 82 GPa indicates the possible lack
269 of B-site Fe³⁺ spin transition. This might be due to that the Mg_{0.88}Fe_{0.1}Al_{0.14}Si_{0.90}O₃ bridgmanite
270 contains ~10% Fe in the A site while 14% Al preferentially stays in the B site (Fu et al., 2019a;
271 Mao et al., 2017).

272 High-pressure aggregate K_S and μ of the Fe10-Al14-Bgm can be fitted using third-order
273 Eulerian finite-strain equations (Stixrude and Lithgow-Bertelloni, 2005):

$$K_S = (1 + 2f)^{5/2} [K_{S0} + (3K_{S0}K'_{S0} - 5K_{S0})f + 13.5(K_{S0}K'_{S0} - 4K_{S0})f^2] \quad (17)$$

$$\mu = (1 + 2f)^{5/2} [\mu_0 + (3K_{S0}\mu'_0 - 5\mu_0)f + (6K_{S0}\mu'_0 - 24K_{S0} - 14\mu_0 + 4.5K_{S0}K'_{S0})f^2] \quad (18)$$

274 where K_{S0} (μ_0) is the adiabatic bulk (shear) modulus at the reference pressure (25 GPa in this study),
275 K'_{S0} (μ'_0) is the pressure derivative of K_{S0} (μ_0). The best fits yield $K_S = 326 (\pm 4) \text{ GPa}$,
276 $\mu = 211 (\pm 2) \text{ GPa}$, and $K'_S = 3.32 (\pm 0.04) \text{ GPa}$, $\mu' = 1.66 (\pm 0.02)$ at 25 GPa (Table 2). These
277 values for Fe10-Al14-Bgm are comparable to literature reports on Al-, Fe-, or (Al,Fe)-bearing
278 bridgmanite (Chantel et al., 2012; Criniti et al., 2021; Jackson et al., 2005; Kurnosov et al., 2017;
279 Murakami et al., 2012) after taking into account Fe and Al substitution effects, pressure effects, as

280 well as trade-offs between elastic moduli and their pressure derivatives during fitting (Figure 6 and
281 Table 3). We note that the reference pressure in literatures is typically at ambient conditions
282 (Chantel et al., 2012; Jackson et al., 2005; Kurnosov et al., 2017), while we used the initial
283 experimental pressure of 25 GPa as the reference. We also note that literature studies (Chantel et al.,
284 2012; Jackson et al., 2005; Kurnosov et al., 2017) commonly neglect the term at f^2 order when
285 evaluating high-pressure elasticity of bridgmanite. Such approximations are acceptable at relatively
286 low pressures (<40 GPa), where the term f^2 is small and neglectable. However, Helmholtz free
287 energy at higher orders increases with pressure and cannot be simply truncated at high P-T
288 conditions (Stixrude and Lithgow-Bertelloni, 2005). In addition, the EoS data from XRD
289 experiments in literature and this study are used to derive the isothermal bulk modulus (K_{T0}), which
290 is slightly different from K_{S0} from velocity measurements even after the K_{S0} - K_{T0} conversion (Table
291 3) (Boffa Ballaran et al., 2012; Criniti et al., 2021; Kurnosov et al., 2017; Mao et al., 2017;
292 Murakami et al., 2012). The sensitivity of the bulk moduli to density and velocity data and their
293 errors with different fitting methods will need further evaluation in understanding the difference.

294 **Effects of Fe and Al substitution on elastic properties of bridgmanite**

295 Studies suggest that Fe and Al cations could enter A-site Mg and B-site Si in the structure of
296 bridgmanite via charge-coupled substitution under lower-mantle P-T and compositional conditions
297 (Irifune et al., 2010; Lin et al., 2013). It is thus important to quantitatively evaluate Fe and Al
298 substitution effects on the elastic properties of bridgmanite aggregates before one can apply
299 elasticity results for lower-mantle implications. Here for a simplicity, we assume that both Fe and
300 Al compositional effects on the K_S and μ of bridgmanite are linear. As to the existence of Fe^{2+} and
301 Fe^{3+} in bridgmanite, we take the total Fe effect as the sum of Fe^{2+} and Fe^{3+} contents. With those
302 assumptions, all the literature high-pressure K_S and μ data of bridgmanite with different

303 compositions (Chantel et al., 2012; Criniti et al., 2021; Fu et al., 2018; Jackson et al., 2005;
304 Kurnosov et al., 2017; Murakami et al., 2012; Murakami et al., 2007) were fit together with the
305 Fe₁₀-Al₁₄-Bgm in this study using third-order Eulerian finite-strain equations (Figure 6). We note
306 that we only included the velocity data of the Fe-bearing bridgmanite by Fu et al. (2018) at 25-40
307 GPa range because of the existence of B-site Fe³⁺ spin transition at 40-60 GPa. The best fits yield:

$$K_{S0}(Fe, Al) = 253 - 118Fe_{Bgm} + 64Al_{Bgm} \quad (19)$$

$$K'_{S0}(Fe, Al) = 4.29 + 0.9Fe_{Bgm} - 6.05Al_{Bgm} \quad (20)$$

$$\mu_0(Fe, Al) = 174.7 - 4.28Fe_{Bgm} - 98.9Al_{Bgm} \quad (21)$$

$$\mu'_0(Fe, Al) = 1.67 + 1.10Fe_{Bgm} + 1.24Al_{Bgm} \quad (22)$$

308 where Fe_{Bgm} and Al_{Bgm} are Fe and Al contents in bridgmanite, calculated as $Fe_{Bgm}=Fe/(Fe+Mg)$
309 and $Al_{Bgm}=Al/(Al+Si)$, respectively. We note that 68% residues of K_S and μ in the best fits are
310 less than 1.1% and 1.0%, respectively ($\pm 1\sigma$) (Figure 6c-d), indicating these evaluations are
311 statistically reliable within uncertainties. The modeled μ_0 and K_{T0} for MgSiO₃ bridgmanite end
312 member are consistent with literature reports within experimental uncertainties (Chantel et al.,
313 2012; Li and Zhang, 2005). The modeling shows that incorporation of Fe into bridgmanite will
314 decrease its K_S and V_P , while Al will increase the K_S and V_P . As to the shear moduli, Al has a
315 much stronger effect on μ and V_S reductions of bridgmanite as compared to Fe incorporation.

316

317

IMPLICATIONS

318 Velocity and density comparisons between seismic observations (Dziewonski and Anderson,
319 1981; Kennett et al., 1995) and mineral physics models (Irifune et al., 2010; Kurnosov et al.,

2017; Mashino et al., 2020; Murakami et al., 2012) have been widely used to constrain the lower-
mantle mineralogy. For instance, Murakami et al. (2012) used V_S of polycrystalline Al-bearing
bridgmanite up to 124 GPa and 2700 K to suggest greater than 92 vol% bridgmanite in the lower
mantle, while Kurnosov et al. (2017) suggested a Fe³⁺-rich pyrolitic lower mantle above 1200-km
depth from single-crystal elasticity data of Fe10-Al10-Bgm up to 40 GPa at 300 K. However, it
has been pointed out by Cottaar et al. (2014) that the conclusion of a perovskitic lower mantle
(Murakami et al., 2012) was not supported because of the use of inconsistent thermoelastic
modeling and inappropriate averaging schemes for mineral aggregates. Here we have adopted a
self-consistent thermoelastic model within the framework of Mie-Grüneisen thermal EoS and
finite-strain theory (Jackson and Rigden, 1996; Stixrude and Lithgow-Bertelloni, 2005) to
evaluate lower-mantle mineralogy at the extended lower-mantle depth.

331 **Modeling of velocity profiles of one-phase bridgmanite in the lower mantle**

332 The high P-T K_S and μ of an individual phase can be calculated using self-consistent
333 thermoelastic equations:

$$P(V, T) = P_{300K} + \gamma \Delta \mathcal{U}_q / V \quad (23)$$

$$K_S(V, T) = K_{S,300K} + (\gamma + 1 - q_0) \gamma \Delta \mathcal{U}_q / V - \gamma^2 \Delta(C_V T) / V \quad (24)$$

$$\mu = \mu_{300K} - \eta_{S0} \Delta \mathcal{U}_q / V \quad (25)$$

334 where P_{300K} , $K_{S,300K}$, and μ_{300K} are pressure, adiabatic bulk moduli, and shear moduli at 300 K,
335 respectively, that can be calculated using Birch-Murnaghan EoS and finite-strain equations
336 (Birch, 1952), q_0 is a volume-independent constant, γ is the Grüneisen parameter, η_{S0} is the shear
337 strain derivative of γ , and $\Delta \mathcal{U}_q$ and $\Delta(C_V T)$ are internal energy and heat differences between 300

338 K and high temperature, respectively. γ and α can be calculated using equations of $\gamma =$
339 $\gamma_0(V/V_0)^{q_0}$ and $\alpha = \frac{1}{V}(\partial V/\partial T)_P$. High P-T U_q and isochoric heat capacity (C_V) can be modeled
340 with Debye approximations:

$$U_q(V, T) = 9nRT \left(\frac{\theta_D}{T}\right)^{-3} \int_0^{\theta_D/T} \frac{x^3}{e^x - 1} dx \quad (26)$$

$$C_V(V, T) = 9nRT \left(\frac{\theta_D}{T}\right)^{-3} \int_0^{\theta_D/T} \frac{x^4 e^x}{(e^x - 1)^2} dx \quad (27)$$

341 where R is the gas constant, n is the number of atoms in the mineral formula, and θ_D is Debye
342 temperature, expressed as:

$$\theta_D = \theta_0 e^{\left(-\frac{\gamma - \gamma_0}{q_0}\right)} \quad (28)$$

343 where θ_0 is the ambient Debye temperature. Four parameters, θ_0 , γ_0 , q_0 , and η_{S0} are involved for
344 the high-temperature extrapolations of velocities. Here, we neglected chemical effects on these
345 parameters for bridgmanite due to limited high P-T experimental data on different compositions.
346 Values of θ_0 , q_0 , γ_0 , and η_{S0} for (Al,Fe)-bearing bridgmanite are constrained as 900 K, 1.57, 1.1,
347 and 2.4, respectively (Table S3), by benchmarking from previous experimental data together
348 with *ab initio* calculations (Fiquet et al., 2000; Shim and Duffy, 2000; Stixrude and Lithgow-
349 Bertelloni, 2005; Tange et al., 2012; Wentzcovitch et al., 2004; Wolf et al., 2015). We note that
350 perturbations to these temperature-related parameters have weak influences on the modeled
351 velocity profiles (Cottaar et al., 2014). For instance, if $\pm 20\%$, $\pm 30\%$, $\pm 50\%$, $\pm 40\%$ perturbations
352 are given to θ_0 , q_0 , γ_0 , and η_{S0} values, respectively, variations in V_P , V_S , and ρ will be less than
353 0.6%.

354 Taking advantage of quantitative Fe and Al effects on elastic properties of bridgmanite as
355 discussed earlier, we modeled velocity profiles of bridgmanite with three compositions along an
356 expected geotherm in the lower mantle (Katsura et al., 2010), including MgSiO₃ end member, Fe5-
357 Al5-Bgm with 5 mol% Fe and Al, and Fe10-Al10-Bgm with 10 mol% Fe and Al. Our modeled
358 results show that the V_P and V_S of MgSiO₃ end member are about 2.9% and 3.7% higher than those
359 of PREM, respectively (Figure 7). With the Fe and Al contents increasing in bridgmanite, both V_P
360 and V_S decrease. For instance, the Fe5-Al5-Bgm has 1-2% higher V_P and V_S than PREM and the
361 Fe10-Al10-Bgm show almost consistent velocities to PREM across the whole lower-mantle depth
362 within uncertainties.

363 Lower-mantle mineralogy from velocity profiles of mineral aggregates

364 To the first order, the lower mantle is believed to be chemically homogenous, adiabatic, and
365 under gravitational self-compression with Bullen's parameter close to one, because of the
366 consistency between 1D seismic profiles (Dziewonski and Anderson, 1981; Kennett et al., 1995)
367 and the Adams-Williamson equation (Williamson and Adams, 1923). With such a simplification,
368 we made the following assumptions to quantitatively estimate the lower-mantle composition: (1)
369 Volume percentages of bridgmanite (V_{Bgm}), ferropericlasite (V_{Fp}), and davemaoite (V_{CaPv}) are
370 constant with depth, where the total is defined as 100%; (2) Total Fe content (Fe) is constant
371 with depth: $Fe = Fe_{Bgm}V_{Bgm} + Fe_{Fp}V_{Fp}$, where Fe_{Bgm} and Fe_{Fp} are Fe contents in bridgmanite
372 and ferropericlasite, respectively; (3) Studies have suggested Fe partitioning coefficient between
373 bridgmanite and ferropericlasite (K_D , given by $[Fe^{2+}+Fe^{3+}]_{Bgm}/[Mg^{2+}]_{Bgm}/(Fe^{2+}]_{Fp}/[Mg^{2+}]_{Fp}$) could
374 vary with depth as a result of the spin crossover in ferropericlasite (Irifune et al., 2010), so we
375 used the K_D value (Figure 8a); (4) Bulk properties of mineral aggregates can be represented using
376 Voigt-Reuss-Hill averages (Hill, 1952). With all these factors considered, we have modeled V_P ,

377 V_S , and ρ profiles of bridgmanite, ferropericlase, and CaSiO_3 davemaoite aggregates along an
378 adiabatic geotherm (Katsura et al., 2010) to best fit with seismic PREM profiles (Dziewonski and
379 Anderson, 1981) from 28 to 120 GPa. Note that we have not included the topmost and lowermost
380 lower-mantle regions because the breakdown of majoritic garnet (Hirose et al., 2001) and large
381 temperature gradients (Kawai and Tsuchiya, 2009) can significantly affect seismic profiles in
382 these regions, respectively. We also note that thermoelastic parameters of ferropericlase and
383 davemaoite for high P-T modeling were constrained by refitting and benchmarking from
384 previous experiments and theoretical calculations (see details in supplementary materials,
385 Figures S2-S3, Table S3) (Fan et al., 2019; Gréaux et al., 2019; Kawai and Tsuchiya, 2015; Li et
386 al., 2006; Sun et al., 2016; Wu et al., 2013; Yang et al., 2016)

387 Our best fits to PREM velocity profiles show a lower-mantle mineralogy of $\sim 88.7(\pm 2.0)$ vol%
388 (Al,Fe)-bearing bridgmanite, $\sim 4.3(\pm 2.0)$ vol% ferropericlase, and 7 vol% (fixed) CaSiO_3
389 davemaoite (Figure 8). In contrast, a pyrolitic model shows lower V_P and V_S profiles than PREM
390 (Figure 8e-f). Because we varied K_D with depth in our best-fit model (Irifune et al., 2010), Fe
391 and Al contents in bridgmanite and ferropericlase can vary accordingly (Figure 8a-b). For the
392 three individual minerals, bridgmanite displays slightly higher velocities than those of PREM,
393 while ferropericlase and CaSiO_3 davemaoite show lower velocities (Figure 8c-d). In comparison,
394 velocities of bridgmanite containing fixed 10 mol% Fe and Al are barely distinguishable with
395 PREM within uncertainties (Figure 7). Specifically, V_S profiles of these minerals are well
396 distinguishable from one another, that makes it the most sensitive elastic parameter to evaluate
397 the lower-mantle mineralogy. V_P softening across the spin crossover in ferropericlase is smeared
398 out because of the high-temperature effect in broadening the transition, but the V_P reduction
399 within the spin crossover is still visible at mid-lower mantle P-T. Notably, the Fe content in the

400 low-spin ferropericlase increases because of the varying K_D with depth (Figure 8b), which in turn
401 flattens V_S toward the deeper lower mantle (Figure 8d). We note that in the best-fit model, we
402 fixed the amount of davemaoite as 7 vol% because of its low abundance in both pyrolitic and
403 chondritic models (McDonough and Sun, 1995). We conducted additional fits to allow K_D and
404 the davemaoite content to vary within 0.33-0.74 and 5-10 vol%, respectively (Figure S4). We
405 found that their variations have limited effects on the derived lower-mantle mineralogy (e.g.,
406 they would cause ~2 vol% variation in bridgmanite content).

407 The modeled high P-T V_P and V_S profiles of mineral aggregates have typical errors of ± 2 -3%
408 at $\pm 1\sigma$ level because of uncertainties involved in experimental data, evaluations of Fe/Al effects,
409 and high P-T extrapolations. Our modeling shows that a pyrolitic model with $+1\sigma$ upper bounds
410 would marginally overlap with PREM profiles (Figure 8e-f). In addition, although we took the
411 adiabatic mantle geotherm from the literature (Katsura et al., 2010) in our model, thermoelastic
412 properties of constituent materials would in turn affect the lower-mantle thermal status. If we
413 assume the lower mantle is superadiabatic with the Bullen's parameter less than 1 (Bunge et al.,
414 2001), it will consequently result in 1-2% decrease in velocities and cause additional mismatches
415 with PREM. Overall, taking all these factors into consideration, even with the most
416 comprehensive study on the single-crystal elasticity of (Al,Fe)-bearing bridgmanite thus far, the
417 uncertainties ($\pm 1\sigma$) in velocity profiles of the lower-mantle bridgmanite are in the order of a few
418 percent. This magnitude would translate into a significant uncertainty of approximately 15 vol%
419 in evaluating the lower-mantle compositions such as pyrolite and chondritic models
420 (McDonough and Sun, 1995; Murakami et al., 2012; Ringwood, 1975). Future high P-T elasticity
421 studies using combined high-quality mineral physics results with approximately 0.1 %

422 uncertainties and high-resolution seismic data are needed to better elucidate spatial and temporal
423 signatures of the mantle geophysics, geodynamics, and geochemistry.

424

425

ACKNOWLEDGEMENTS

426 The authors acknowledge S. Grand, I. Jackson, R. Wentzcovitch, and C. Liu for constructive
427 discussions. The authors appreciate V. Prakapenka and E. Greenberg for helping with X-ray
428 diffraction experiments at 13ID-D, GSECARS. GSECARS was supported by the National Science
429 Foundation (EAR-1128799) and U.S. Department of Energy, Geosciences (DE-FG02-94ER14466).
430 J.F. Lin acknowledges support from National Science Foundation Geophysics Program (EAR-
431 2001381 & EAR-1916941) and the Joint Use/Research Program of the Institute for Planetary
432 Materials, Okayama University. T. Okuchi acknowledges support from JSPS KAKENHI
433 (17H01172).

434 Competing interests

435 The authors declare no competing interests.

436

437

References

438 Allègre, C.J., Poirier, J.-P., Humler, E., Hofmann, A.W., 1995. The chemical composition of the
439 Earth. *Earth and Planetary Science Letters* 134, 515-526.
440 Birch, F., 1952. Elasticity and Constitution of the Earth Interior. *Journal of Geophysical*
441 *Research* 57, 227-286.
442 Boffa Ballaran, T., Kurnosov, A., Glazyrin, K., Frost, D.J., Merlini, M., Hanfland, M., Caracas, R.,
443 2012. Effect of chemistry on the compressibility of silicate perovskite in the lower mantle.
444 *Earth and Planetary Science Letters* 333, 181-190.
445 Bunge, H.P., Ricard, Y., Matas, J., 2001. Non-adiabaticity in mantle convection. *Geophysical*
446 *research letters* 28, 879-882.

- 447 Chantel, J., Frost, D.J., McCammon, C.A., Jing, Z.C., Wang, Y.B., 2012. Acoustic velocities of
448 pure and iron-bearing magnesium silicate perovskite measured to 25 GPa and 1200 K.
449 Geophysical Research Letters 39.
- 450 Cottaar, S., Heister, T., Rose, I., Unterborn, C., 2014. BurnMan: A lower mantle mineral
451 physics toolkit. *Geochemistry, Geophysics, Geosystems* 15, 1164-1179.
- 452 Criniti, G., Kurnosov, A., Boffa Ballaran, T., Frost, D.J., 2021. Single-Crystal Elasticity of
453 MgSiO₃ Bridgmanite to Mid-Lower Mantle Pressure. *Journal of Geophysical Research: Solid
454 Earth* 126, e2020JB020967.
- 455 Dewaele, A., Loubeyre, P., Mezouar, M., 2004. Equations of state of six metals above 94 GPa.
456 *Physical Review B* 70, 094112.
- 457 Dziewonski, A.M., Anderson, D.L., 1981. Preliminary Reference Earth Model. *Physics of the
458 Earth and Planetary Interiors* 25, 297-356.
- 459 Every, A., 1980. General closed-form expressions for acoustic waves in elastically
460 anisotropic solids. *Physical Review B* 22, 1746.
- 461 Fan, D., Fu, S., Yang, J., Tkachev, S.N., Prakapenka, V.B., Lin, J.-F., 2019. Elasticity of single-
462 crystal periclase at high pressure and temperature: The effect of iron on the elasticity and
463 seismic parameters of ferropericlase in the lower mantle. *American Mineralogist: Journal of
464 Earth and Planetary Materials* 104, 262-275.
- 465 Fiquet, G., Dewaele, A., Andrault, D., Kunz, M., Le Bihan, T., 2000. Thermoelastic properties
466 and crystal structure of MgSiO₃ perovskite at lower mantle pressure and temperature
467 conditions. *Geophysical Research Letters* 27, 21-24.
- 468 Frost, D.J., Liebske, C., Langenhorst, F., McCammon, C.A., Trønnes, R.G., Rubie, D.C., 2004.
469 Experimental evidence for the existence of iron-rich metal in the Earth's lower mantle.
470 *Nature* 428, 409.
- 471 Fu, S., Yang, J., Karato, S.i., Vasiliev, A., Presniakov, M.Y., Gavrilliuk, A.G., Ivanova, A.G., Hauri,
472 E.H., Okuchi, T., Purevjav, N., Lin, J.F., 2019a. Water concentration in single-crystal (Al, Fe)-
473 bearing bridgmanite grown from the hydrous melt: implications for dehydration melting at
474 the topmost lower mantle. *Geophysical Research Letters* 46, 10346-10357.
- 475 Fu, S., Yang, J., Tsujino, N., Okuchi, T., Purevjav, N., Lin, J.F., 2019b. Single-crystal elasticity of
476 (Al,Fe)-bearing bridgmanite and seismic anisotropy at the topmost lower mantle. *Earth and
477 Planetary Science Letters* 518, 116-126.
- 478 Fu, S., Yang, J., Zhang, Y., Okuchi, T., McCammon, C., Kim, H.I., Lee, S.K., Lin, J.F., 2018.
479 Abnormal Elasticity of Fe-Bearing Bridgmanite in the Earth's Lower Mantle. *Geophysical
480 Research Letters* 45, 4725-4732.
- 481 Fukui, H., Yoneda, A., Nakatsuka, A., Tsujino, N., Kamada, S., Ohtani, E., Shatskiy, A., Hirao, N.,
482 Tsutsui, S., Uchiyama, H., 2016. Effect of cation substitution on bridgmanite elasticity: A key
483 to interpret seismic anomalies in the lower mantle. *Scientific reports* 6, 33337.
- 484 Gréaux, S., Irifune, T., Higo, Y., Tange, Y., Arimoto, T., Liu, Z., Yamada, A., 2019. Sound
485 velocity of CaSiO₃ perovskite suggests the presence of basaltic crust in the Earth's lower
486 mantle. *Nature* 565, 218.
- 487 Hill, R., 1952. The Elastic Behaviour of a Crystalline Aggregate. *Proceedings of the Physical
488 Society of London Section B* 65, 349.
- 489 Hirose, K., Fei, Y., Ono, S., Yagi, T., Funakoshi, K.-i., 2001. In situ measurements of the phase
490 transition boundary in Mg₃Al₂Si₃O₁₂: implications for the nature of the seismic
491 discontinuities in the Earth's mantle. *Earth and Planetary Science Letters* 184, 567-573.

- 492 Hofmann, A.W., 1997. Mantle geochemistry: the message from oceanic volcanism. *Nature*
493 385, 219.
- 494 Irifune, T., Shinmei, T., McCammon, C.A., Miyajima, N., Rubie, D.C., Frost, D.J., 2010. Iron
495 partitioning and density changes of pyrolite in Earth's lower mantle. *Science* 327, 193-195.
- 496 Jackson, I., Rigden, S.M., 1996. Analysis of PVT data: constraints on the thermoelastic
497 properties of high-pressure minerals. *Physics of the earth and planetary interiors* 96, 85-
498 112.
- 499 Jackson, J.M., Zhang, J., Shu, J., Sinogeikin, S.V., Bass, J.D., 2005. High-pressure sound
500 velocities and elasticity of aluminous MgSiO₃ perovskite to 45 GPa: Implications for lateral
501 heterogeneity in Earth's lower mantle. *Geophysical Research Letters* 32.
- 502 Karki, B., Stixrude, L., Clark, S., Warren, M., Ackland, G., Crain, J., 1997. Elastic properties of
503 orthorhombic MgSiO₃ perovskite at lower mantle pressures. *American Mineralogist* 82,
504 635-638.
- 505 Katsura, T., Yoneda, A., Yamazaki, D., Yoshino, T., Ito, E., 2010. Adiabatic temperature profile
506 in the mantle. *Physics of the Earth and Planetary Interiors* 183, 212-218.
- 507 Kawai, K., Tsuchiya, T., 2009. Temperature profile in the lowermost mantle from
508 seismological and mineral physics joint modeling. *Proceedings of the National Academy of*
509 *Sciences* 106, 22119-22123.
- 510 Kawai, K., Tsuchiya, T., 2015. Small shear modulus of cubic CaSiO₃ perovskite. *Geophysical*
511 *Research Letters* 42, 2718-2726.
- 512 Kennett, B.L.N., Engdahl, E.R., Buland, R., 1995. Constraints on Seismic Velocities in the
513 Earth from Travel-Times. *Geophysical Journal International* 122, 108-124.
- 514 Kurnosov, A., Marquardt, H., Frost, D., Ballaran, T.B., Ziberna, L., 2017. Evidence for a Fe³⁺-
515 rich pyrolitic lower mantle from (Al, Fe)-bearing bridgmanite elasticity data. *Nature* 543,
516 543-546.
- 517 Kurnosov, A., Marquardt, H., Frost, D.J., Ballaran, T.B., Ziberna, L., 2018. Kurnosov et al.
518 reply. *Nature* 564, E27-E31.
- 519 Li, B.S., Zhang, J.Z., 2005. Pressure and temperature dependence of elastic wave velocity of
520 MgSiO₃ perovskite and the composition of the lower. *Physics of the Earth and Planetary*
521 *Interiors* 151, 143-154.
- 522 Li, L., Brodholt, J.P., Stackhouse, S., Weidner, D.J., Alfredsson, M., Price, G.D., 2005. Elasticity
523 of (Mg,Fe)(Si,Al)O₃-perovskite at high pressure. *Earth and Planetary Science Letters* 240,
524 529-536.
- 525 Li, L., Weidner, D.J., Brodholt, J., Alfe, D., Price, G.D., Caracas, R., Wentzcovitch, R., 2006.
526 Elasticity of CaSiO₃ perovskite at high pressure and high temperature. *Physics of the Earth*
527 *and Planetary Interiors* 155, 249-259.
- 528 Lin, J.-F., Mao, Z., Yang, J., Fu, S., 2018. Elasticity of lower-mantle bridgmanite. *Nature* 564,
529 E18-E26.
- 530 Lin, J.F., Speziale, S., Mao, Z., Marquardt, H., 2013. Effects of the Electronic Spin Transitions
531 of Iron in Lower Mantle Minerals: Implications for Deep Mantle Geophysics and
532 Geochemistry. *Reviews of Geophysics* 51, 244-275.
- 533 Lundin, S., Catalli, K., Santillan, J., Shim, S.H., Prakapenka, V.B., Kunz, M., Meng, Y., 2008.
534 Effect of Fe on the equation of state of mantle silicate perovskite over 1 Mbar. *Physics of the*
535 *Earth and Planetary Interiors* 168, 97-102.

- 536 Mao, Z., Lin, J.F., Liu, J., Prakapenka, V.B., 2011. Thermal equation of state of lower-mantle
537 ferropericlase across the spin crossover. *Geophysical Research Letters* 38.
- 538 Mao, Z., Wang, F., Lin, J.-F., Fu, S., Yang, J., Wu, X., Okuchi, T., Tomioka, N., Prakapenka, V.B.,
539 Xiao, Y., 2017. Equation of state and hyperfine parameters of high-spin bridgmanite in the
540 Earth's lower mantle by synchrotron X-ray diffraction and Mössbauer spectroscopy.
541 *American Mineralogist* 102, 357-368.
- 542 Marquardt, H., Marquardt, K., 2012. Focused ion beam preparation and characterization of
543 single-crystal samples for high-pressure experiments in the diamond-anvil cell. *American*
544 *Mineralogist* 97, 299-304.
- 545 Marquardt, H., Speziale, S., Reichmann, H.J., Frost, D.J., Schilling, F.R., 2009. Single-crystal
546 elasticity of $(\text{Mg}_{0.9}\text{Fe}_{0.1})\text{O}$ to 81 GPa. *Earth and Planetary Science Letters* 287, 345-352.
- 547 Mashino, I., Murakami, M., Miyajima, N., Petitgirard, S., 2020. Experimental evidence for
548 silica-enriched Earth's lower mantle with ferrous iron dominant bridgmanite. *Proceedings*
549 *of the National Academy of Sciences* 117, 27899-27905.
- 550 McCammon, C., 1997. Perovskite as a possible sink for ferric iron in the lower mantle.
551 *Nature* 387, 694.
- 552 McDonough, W.F., Sun, S.-S., 1995. The composition of the Earth. *Chemical geology* 120,
553 223-253.
- 554 Murakami, M., Ohishi, Y., Hirao, N., Hirose, K., 2012. A perovskitic lower mantle inferred
555 from high-pressure, high-temperature sound velocity data. *Nature* 485, 90-94.
- 556 Murakami, M., Sinogeikin, S.V., Hellwig, H., Bass, J.D., Li, J., 2007. Sound velocity of MgSiO_3
557 perovskite to Mbar pressure. *Earth Planet Sc Lett* 256, 47-54.
- 558 Ringwood, A.E., 1975. Composition and petrology of the earth's mantle [by] AE Ringwood.
- 559 Shim, S.-H., Duffy, T.S., 2000. Constraints on the PVT equation of state of MgSiO_3 perovskite.
560 *American Mineralogist* 85, 354-363.
- 561 Shukla, G., Cococcioni, M., Wentzcovitch, R.M., 2016. Thermoelasticity of Fe^{3+} -and Al-
562 bearing bridgmanite: Effects of iron spin crossover. *Geophysical Research Letters* 43, 5661-
563 5670.
- 564 Shukla, G., Wentzcovitch, R.M., 2016. Spin crossover in $(\text{Mg},\text{Fe}^{3+})(\text{Si},\text{Fe}^{3+})\text{O}_3$ bridgmanite:
565 Effects of disorder, iron concentration, and temperature. *Physics of the Earth and Planetary*
566 *Interiors* 260, 53-61.
- 567 Speziale, S., Marquardt, H., Duffy, T.S., 2014. Brillouin scattering and its application in
568 geosciences. *Reviews in Mineralogy and Geochemistry* 78, 543-603.
- 569 Stixrude, L., Lithgow-Bertelloni, C., 2005. Thermodynamics of mantle minerals—I. Physical
570 properties. *Geophysical Journal International* 162, 610-632.
- 571 Sun, N., Mao, Z., Yan, S., Wu, X., Prakapenka, V.B., Lin, J.F., 2016. Confirming a pyrolitic lower
572 mantle using self-consistent pressure scales and new constraints on CaSiO_3 perovskite.
573 *Journal of Geophysical Research: Solid Earth* 121, 4876-4894.
- 574 Tange, Y., Kuwayama, Y., Irifune, T., Funakoshi, K.i., Ohishi, Y., 2012. P-V-T equation of state
575 of MgSiO_3 perovskite based on the MgO pressure scale: A comprehensive reference for
576 mineralogy of the lower mantle. *Journal of Geophysical Research: Solid Earth* 117.
- 577 Thomson, A.R., Crichton, W.A., Brodholt, J.P., Wood, I.G., Siersch, N.C., Muir, J.M.R., Dobson,
578 D.P., Hunt, S.A., 2019. Seismic velocities of CaSiO_3 perovskite can explain LLSVPs in Earth's
579 lower mantle. *Nature*.

580 Tschauner, O., Huang, S., Yang, S., Humayun, M., Liu, W., Gilbert Corder, S.N., Bechtel, H.A.,
581 Tischler, J., Rossman, G., 2021. Discovery of davemaoite, CaSiO₃-perovskite, as a mineral
582 from the lower mantle. *Science* 374, 891-894.
583 Wentzcovitch, R., Karki, B., Cococcioni, M., De Gironcoli, S., 2004. Thermoelastic Properties
584 of MgSiO₃-Perovskite: Insights on the Nature of the Earth's Lower Mantle. *Physical review*
585 *letters* 92, 018501.
586 Williamson, E.D., Adams, L.H., 1923. Density distribution in the Earth. *Journal of the*
587 *Washington Academy of Sciences* 13, 413-428.
588 Wolf, A.S., Jackson, J.M., Dera, P., Prakapenka, V.B., 2015. The thermal equation of state of
589 (Mg,Fe)SiO₃ bridgmanite (perovskite) and implications for lower mantle structures. *Journal*
590 *of Geophysical Research-Solid Earth* 120, 7460-7489.
591 Wu, Z.Q., Justo, J.F., Wentzcovitch, R.M., 2013. Elastic Anomalies in a Spin-Crossover System:
592 Ferroperriclite at Lower Mantle Conditions. *Physical Review Letters* 110.
593 Xu, S., Lin, J.F., Morgan, D., 2017. Iron partitioning between ferroperriclite and bridgmanite
594 in the Earth's lower mantle. *Journal of Geophysical Research: Solid Earth* 122, 1074-1087.
595 Yang, J., Lin, J.F., Jacobsen, S.D., Seymour, N.M., Tkachev, S.N., Prakapenka, V.B., 2016.
596 Elasticity of ferroperriclite and seismic heterogeneity in the Earth's lower mantle. *Journal*
597 *of Geophysical Research: Solid Earth*.
598 Yang, J., Tong, X.Y., Lin, J.F., Okuchi, T., Tomioka, N., 2015. Elasticity of Ferroperriclite across
599 the Spin Crossover in the Earth's Lower Mantle. *Scientific Reports* 5.
600 Yeganeh-Haeri, A., 1994. Synthesis and re-investigation of the elastic properties of single-
601 crystal magnesium silicate perovskite. *Physics of the Earth and Planetary Interiors* 87, 111-
602 121.

603

604

605 **List of figure captions:**

606 **Figure 1.** Sensitivity analyses of single-crystal bridgmanite platelets for derivations of its elastic
607 moduli. (a) and (b) Platelets with crystallographic orientations of (-0.50, 0.05, -0.86) and (0.65, -
608 0.59, 0.48), respectively. The calculations follow literature studies (Fu et al., 2019b; Lin et al., 2018)
609 for analyzing sensitivity of nine C_{ij} to experimentally measured V_P , V_{S1} , and V_{S2} in the
610 orthorhombic-structured single-crystal bridgmanite with a selected orientation.

611 **Figure 2.** High-pressure X-ray diffraction and sound velocity measurements on single-crystal Fe10-
612 Al14-Bgm. (a) Original XRD image on single-crystal Fe10-Al14-Bgm at ~76 GPa and 300 K. (b)
613 The corresponding integrated pattern. In (a), diffraction peaks from the sample are marked with a
614 small rectangle, and signals from neon pressure medium and diamonds are labeled with "neon" and
615 "D", respectively. Analyses of the XRD pattern indicate the loaded platelet has a crystallographic
616 orientation of (-0.50, 0.05, -0.86). In (b), Miller indices (hkl) of bridgmanite are labeled close to
617 diffracted peaks. Average FWHM of these peaks are ~0.06°. Insert in (b) is a zoom-in region

618 marked by a red rectangle in (a), showing nice and round diffraction peaks. (c)-(e) Representative
619 BLS, ISLS, and power spectra of single-crystal Fe10-Al14-Bgm at ~82 GPa and 300 K. Open
620 circles in (c) are raw BLS data and red lines are best fits to derive V_{S1} and V_{S2} . A time-domain ISLS
621 spectrum in (d) is Fourier-transformed into a frequency-domain power spectrum in (e) to derive V_P .
622 The insert in (c) shows an image of the sample chamber with the Fe10-Al14-Bgm platelet and a
623 ruby sphere as the pressure calibrant.

624 **Figure 3.** Sound velocities of single-crystal Fe10-Al14-Bgm as a function of azimuthal chi angles
625 at high pressure. (a) 25.0 GPa. (b) 54.4 GPa. (c) 82.0 GPa. Black and red circles are experimentally
626 measured sound velocities of two platelets with crystallographic orientations of (-0.50, 0.05, -0.86)
627 and (0.65, -0.59, 0.48), respectively. Lines are the best fits to derive the full elastic moduli using
628 Christoffel's equations. The two perpendicularly polarized shear wave velocities, V_{S1} and V_{S2} , are
629 plotted as dashed and solid lines, respectively.

630 **Figure 4.** Single-crystal elastic moduli of Fe10-Al14-Bgm as a function of pressure. Solid red
631 circles are C_{ij} results of Fe10-Al14-Bgm in this study, and solid red lines are the best fits to the data
632 using a finite-strain theory (Stixrude and Lithgow-Bertelloni, 2005). Literature results on
633 bridgmanite with different compositions are plotted for comparisons. Dashed black (Karki et al.,
634 1997), red (Wentzcovitch et al., 2004), blue (Li et al., 2005) lines are from *ab initio* calculations for
635 MgSiO₃ bridgmanite. Other symbols are from previous experimental measurements. Open and solid
636 gray circles: MgSiO₃ bridgmanite from the individual fit and global fit, respectively, and the solid
637 gray lines are the best finite-strain fits (Criniti et al., 2021); solid orange and purple circles: Fe6-
638 Al4-Bgm and Fe12-Al11-Bgm, respectively (Fu et al., 2019b); open black circles: Fe10-Al10-Bgm
639 using the global fit (Kurnosov et al., 2017); solid olive circles: recalculated individual fit results by
640 Lin et al. (2018) using velocity data of Kurnosov et al. (2017); open blue squares: MgSiO₃
641 bridgmanite (Yeganeh-Haeri, 1994); solid black circles: MgSiO₃ bridgmanite (Fukui et al., 2016).
642 Errors are smaller than symbols when not shown.

643 **Figure 5.** Aggregate sound velocities of single-crystal Fe10-Al14-Bgm at high pressure and room
644 temperature. (a) V_P . (b) V_S . Solid red symbols are aggregate velocity calculated from single-crystal
645 C_{ij} of Fe10-Al14-Bgm in this study, and solid red lines are the best fits using a finite-strain theory
646 (Stixrude and Lithgow-Bertelloni, 2005). Other symbols and lines are literature data for different
647 bridgmanite compositions. Particularly, circles are data from single-crystal bridgmanite and
648 triangles and dashed lines are from polycrystalline samples. Open and solid gray circles: single-
649 crystal MgSiO₃ bridgmanite from individual and global fits, respectively, and the solid gray lines
650 are the best finite-strain fits (Criniti et al., 2021); open black circles: single-crystal
651 Mg_{0.9}Fe_{0.1}Si_{0.9}Al_{0.1}O₃ with $Fe^{3+}/\Sigma Fe=0.67$ from the global fit (Kurnosov et al., 2017); solid olive
652 circles: recalculated results by Lin et al. (2018) using the individual fit to the velocity data of
653 Kurnosov et al. (2017); black and orange triangles: polycrystalline MgSiO₃ and Mg_{0.95}Fe_{0.05}SiO₃
654 with $Fe^{3+}/\Sigma Fe=0.2$, respectively (Chantel et al., 2012); dashed blue, olivine, and orange lines:
655 polycrystalline MgSiO₃ (Murakami et al., 2007), Mg_{0.96}Fe_{0.05}Si_{0.99}O₃ (Fu et al., 2018) and Al-
656 bearing bridgmanite containing 5.1 wt% Al₂O₃ (Jackson et al., 2005), respectively. Uncertainties
657 are smaller than symbols when not shown.

658 **Figure 6.** Adiabatic bulk and shear moduli of bridgmanite with different Fe and Al contents at high
659 pressure and 300 K. (a) and (b) K_S and μ , respectively. Solid red circles are from the single-crystal
660 Fe10-Al14-Bgm data in this study and other symbols are experimental data from the literature
661 (Boffa Ballaran et al., 2012; Chantel et al., 2012; Criniti et al., 2021; Fu et al., 2018; Jackson et al.,
662 2005; Kurnosov et al., 2017; Li and Zhang, 2005; Lundin et al., 2008; Mao et al., 2017; Murakami
663 et al., 2012; Murakami et al., 2007). Uncertainties are smaller than symbols when not shown. See
664 detailed references in legends. Solid lines with corresponding colors are the best fits to the data
665 using third-order finite-strain equations (Stixrude and Lithgow-Bertelloni, 2005) that take Fe and Al
666 substitution effects into account. (c) and (d) $\Delta K_S/K_S$ and $\Delta\mu/\mu$, respectively. These are residues in
667 adiabatic bulk and shear moduli between experimental data and the best fits.

668 **Figure 7.** Modeled velocity profiles of bridgmanite at lower-mantle relevant pressure-temperature
669 conditions. Using the quantitative Fe and Al effects on elastic properties of bridgmanite, we
670 modeled V_P and V_S of three bridgmanite compositions, $MgSiO_3$ end member (black lines), Fe5-Al5-
671 Bgm with 5 mol% Fe and Al (blue lines), and Fe10-Al10-Bgm with 10 mol% Fe and Al (red lines)
672 along an expected adiabatic geotherm (Katsura et al., 2010). PREM profiles (Dziewonski and
673 Anderson, 1981) are plotted as open circles for comparison. Vertical ticks show one standard
674 deviation ($\pm 1\sigma$) derived from standard error propagations in the modelling.

675 **Figure 8.** Lower-mantle mineralogy in the best-fit to seismic PREM profiles. (a) Iron partitioning
676 between ferripericlase and bridgmanite (K_D). The dashed black line is from experiments (Irifune et
677 al., 2010) used in this study and shaded orange area is from a theoretical report (Xu et al., 2017). (b)
678 Cation numbers of Fe and Al in bridgmanite and/or ferripericlase with depth. (c) and (d) P-wave
679 and S-wave velocities of individual phases, respectively, in our best-fit model. Solid black, olive
680 and blue lines are for (Al,Fe)-bearing bridgmanite, ferripericlase, and davemaoite, respectively.
681 The Fe/Al contents in bridgmanite/ferripericlase change with depth, shown in (b). Velocities of
682 individual phase were modeled along an adiabatic geotherm (Katsura et al., 2010). PREM profiles
683 (Dziewonski and Anderson, 1981) are plotted as open circles. (e) and (f) P-wave and S-wave
684 velocities of mineral aggregates, respectively. Solid red lines are our best-fits to PREM
685 (Dziewonski and Anderson, 1981). Modeled results for a pyrolitic lower mantle (Irifune et al., 2010)
686 are plotted as dashed red lines. Our best-fit model shows the lower mantle is composed of
687 $\sim 88.7(\pm 2.0)$ vol% bridgmanite, $\sim 4.3(\pm 2.0)$ vol% ferripericlase, and 7 vol% (fixed) $CaSiO_3$
688 davemaoite. Vertical ticks show one standard deviation ($\pm 1\sigma$) derived from standard error
689 propagations in the modelling.

690
691

Table 1. Elastic moduli of single-crystal Fe10-Al14-Bgm at high pressures. Errors in parentheses are one standard deviation ($\pm 1\sigma$) from standard error propagation analyses.

Pressure (GPa)	25.0(3)	35.0(5)	45.0(5)	54.4(6)	65.8(8)	70.4(7)	76.0(9)	82.0(14)
C_{11} (GPa)	542(9)	596(15)	654(15)	693(16)	743(16)	760(15)	773(17)	800(23)
C_{22} (GPa)	653(3)	697(5)	740(4)	791(5)	829(4)	852(5)	860(6)	868(8)
C_{33} (GPa)	598(9)	636(13)	687(14)	744(15)	793(14)	839(16)	895(18)	922(22)
C_{44} (GPa)	207(2)	223(3)	246(2)	256(3)	276(2)	279(3)	295(5)	306(6)
C_{55} (GPa)	213(5)	221(7)	235(6)	242(6)	246(7)	250(9)	249(10)	258(12)
C_{66} (GPa)	235(3)	253(3)	270(3)	285(4)	299(3)	303(4)	311(4)	316(5)
C_{12} (GPa)	162(5)	186(3)	198(5)	204(6)	218(5)	225(6)	227(6)	229(5)
C_{13} (GPa)	192(4)	212(6)	224(6)	250(5)	245(5)	264(7)	278(8)	280(9)
C_{23} (GPa)	225(5)	247(8)	260(8)	290(12)	329(10)	340(13)	376(14)	390(20)
K_S (GPa)	326(4)	356(5)	382(6)	412(6)	437(8)	455(8)	473(9)	485(11)
μ (GPa)	211(2)	224(2)	242(2)	254(2)	268(3)	273(3)	279(4)	287(5)
ρ (g/cm ³)	4.56(1)	4.71(1)	4.83(1)	4.94(2)	5.05(2)	5.10(2)	5.16(2)	5.21(3)
V_P (km/s)	11.52(8)	11.80(8)	12.08(10)	12.33(11)	12.54(12)	12.67(13)	12.79(14)	12.90(16)
V_S (km/s)	6.79(4)	6.90(4)	7.09(5)	7.18(5)	7.28(5)	7.32(5)	7.35(6)	7.42(6)

692 **Table 2.** Pressure derivatives of single-crystal elasticity (C_{ij} , K_S , and μ) of Fe10-Al14-Bgm using a
 693 finite-strain theory. *: The reference pressure is 25 GPa; #: The reference pressure is at ambient
 694 conditions.

Fe10-Al14-Bgm (this study)*			MgSiO ₃ (Criniti et al., 2021)#		
ij	C_{ij0} (GPa)	C'_{ij0}	C_{ij0} (GPa)	C'_{ij0}	
11	542(9)	5.35(9)	487(2)	5.21(9)	
22	653(3)	4.98(14)	524(3)	6.35(6)	
33	598(9)	6.67(28)	467.7(16)	6.56(6)	
44	207(2)	2.01(6)	202.3(2)	1.95(1)	
55	213(5)	1.11(5)	180.2(4)	1.55(1)	
66	235(3)	1.78(3)	141.9(5)	2.30(1)	
12	162(5)	1.58(7)	124.3(18)	3.27(7)	
13	192(4)	1.85(8)	140.9(13)	2.17(6)	
23	225(5)	2.95(12)	152.6(10)	2.22(3)	
	M_0 (GPa)	M'_0	M_0 (GPa)	M'_0	M''_0 (GPa ⁻¹)
K^V	328(4)	3.35(5)	257.1(6)	3.71(4)	-0.014
μ^V	212(2)	1.67(2)	175.6(2)	1.86(1)	-0.0174
K^R	325(4)	3.29(4)	256.7(4)	3.70(3)	-0.014
μ^R	210(2)	1.65(2)	174.0(6)	1.86(4)	-0.0173
K^{VRH}	326(4)	3.32(4)	256.9(8)	3.70(5)	-0.014
μ^{VRH}	211(2)	1.66(2)	174.8(7)	1.86(4)	-0.0174

695

696

697 **Table 3.** Comparisons of bulk and shear moduli of bridgmanite and their pressure derivatives at room temperature. *: The reference pressure is 25 GPa.

Brillouin Light Scattering	Composition	K_{S0} (GPa)	μ_0 (GPa)	K'_{S0}	μ'_0
This study*	$\text{Mg}_{0.93}\text{Fe}^{3+}_{0.048}\text{Fe}^{2+}_{0.032}\text{Al}_{0.10}\text{Si}_{0.90}\text{O}_3$	326(4)	211(2)	3.32(4)	1.66(2)
Fu et al. (2018)	$\text{Mg}_{0.96(1)}\text{Fe}^{2+}_{0.036(5)}\text{Fe}^{3+}_{0.014(5)}\text{Si}_{0.99(1)}\text{O}_3$ (<42.6 GPa)	254(8)	166.2(5)	3.3(3)	1.91(2)
Fu et al. (2018)	$\text{Mg}_{0.96(1)}\text{Fe}^{2+}_{0.036(5)}\text{Fe}^{3+}_{0.014(5)}\text{Si}_{0.99(1)}\text{O}_3$ (> 58 GPa)	234(11)	190.0(7)	3.5(4)	1.54(11)
Jackson et al. (2005)	Al-Bgm (5.1 wt.% Al_2O_3)	252(5)	165(2)	3.7(3)	1.7(2)
Murakami et al. (2007)	MgSiO_3		172.9(2)		1.56(4)
Murakami et al. (2012)	Al-Bgm (4 wt.% Al_2O_3)		166(1)		1.57(5)
Kurnosov et al. (2017)	$(\text{Mg}_{0.9}\text{Fe}_{0.1}\text{Al}_{0.1}\text{Si}_{0.9})\text{O}_3$	250.8(4)	159.7(2)	3.44(3)	2.05(2)
Criniti et al. (2021)	MgSiO_3	257.1(6)	175.6(2)	3.71(4)	1.86(1)
Ultrasonic Interferometry	Composition	K_{S0} (GPa)	μ_0 (GPa)	K'_{S0}	μ'_0
Li and Zhang (2005)	MgSiO_3	253(2)	173(1)	4.4(1)	2.0(1)
Chantel et al. (2012)	MgSiO_3	247(4)	176(2)	4.5(2)	1.6(1)
Chantel et al. (2012)	$(\text{Mg}_{0.95}\text{Fe}_{0.05})\text{SiO}_3$	236(2)	174(1)	4.7(1)	1.56(5)
X-Ray Diffraction	Composition	K_{T0} (GPa)		K'_{T0}	
This study	$\text{Mg}_{0.93}\text{Fe}^{3+}_{0.048}\text{Fe}^{2+}_{0.032}\text{Al}_{0.10}\text{Si}_{0.90}\text{O}_3$	256(2)		4 (fixed)	
Fu et al. (2018)	$\text{Mg}_{0.96(1)}\text{Fe}^{2+}_{0.036(5)}\text{Fe}^{3+}_{0.014(5)}\text{Si}_{0.99(1)}\text{O}_3$ (<40 GPa)	258(1)		4 (fixed)	
Fu et al. (2018)	$\text{Mg}_{0.96(1)}\text{Fe}^{2+}_{0.036(5)}\text{Fe}^{3+}_{0.014(5)}\text{Si}_{0.99(1)}\text{O}_3$ (>60 GPa)	252(2)		4 (fixed)	
Chantel et al. (2012)	MgSiO_3	257(2)		4 (fixed)	
Chantel et al. (2012)	$(\text{Mg}_{0.95}\text{Fe}_{0.05})\text{SiO}_3$	246(2)		4 (fixed)	
Boffa Ballaran et al. (2012)	MgSiO_3	251(2)		4.11(7)	
Boffa Ballaran et al. (2012)	$(\text{Mg}_{0.95}\text{Fe}_{0.05})\text{SiO}_3$	253(3)		3.99(7)	
Boffa Ballaran et al. (2012)	$(\text{Mg}_{0.6}\text{Fe}_{0.4})(\text{Al}_{0.36}\text{Si}_{0.62})\text{O}_3$	240(2)		4.12(8)	
Mao et al. (2017)	$(\text{Mg}_{0.94}\text{Fe}_{0.06})(\text{Al}_{0.01}\text{Si}_{0.99})\text{O}_3$	255(2)		4 (fixed)	
Mao et al. (2017)	$(\text{Mg}_{0.89}\text{Fe}_{0.11})(\text{Al}_{0.11}\text{Si}_{0.89})\text{O}_3$	264(2)		4 (fixed)	

698

Figure 1

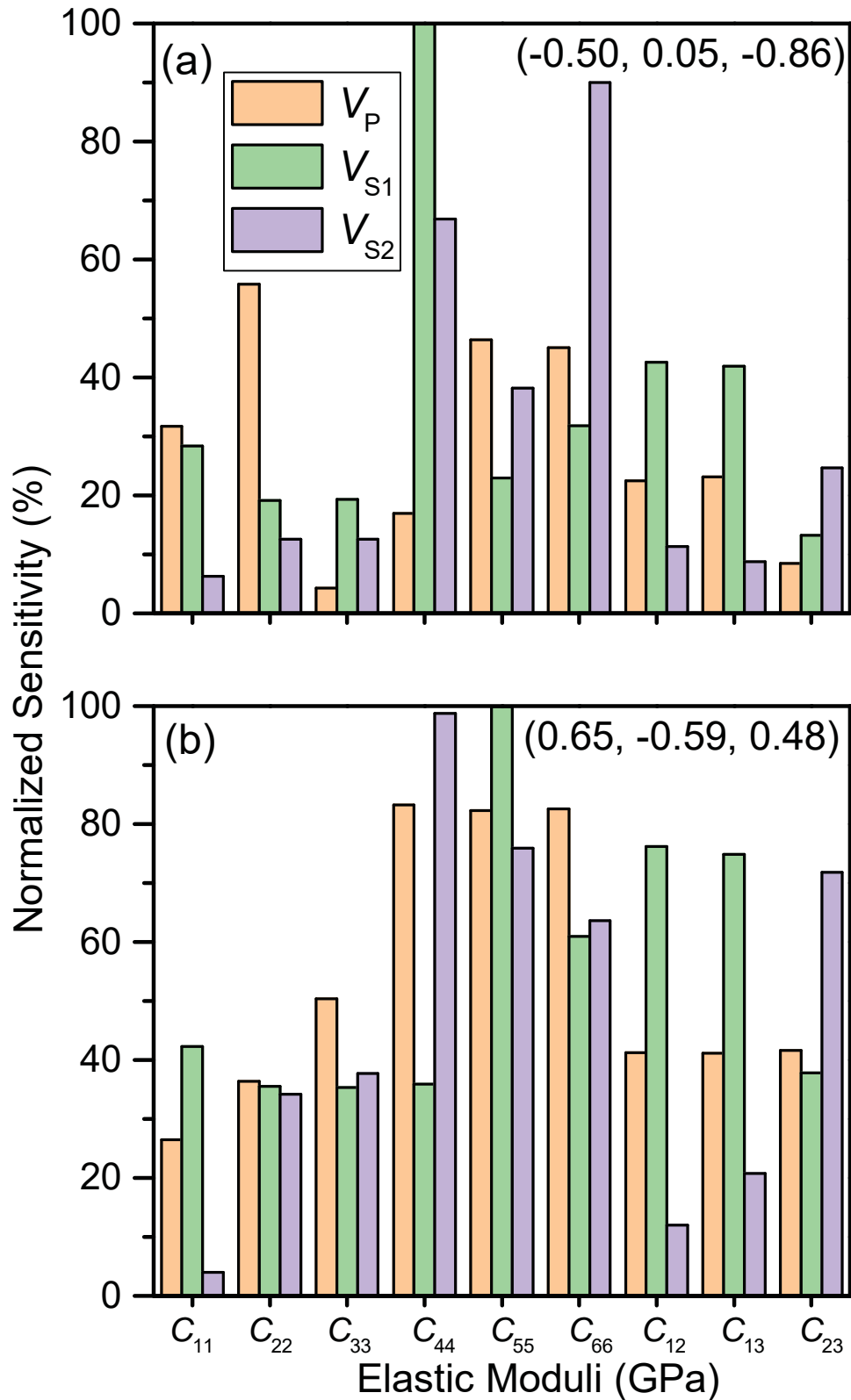


Figure 2

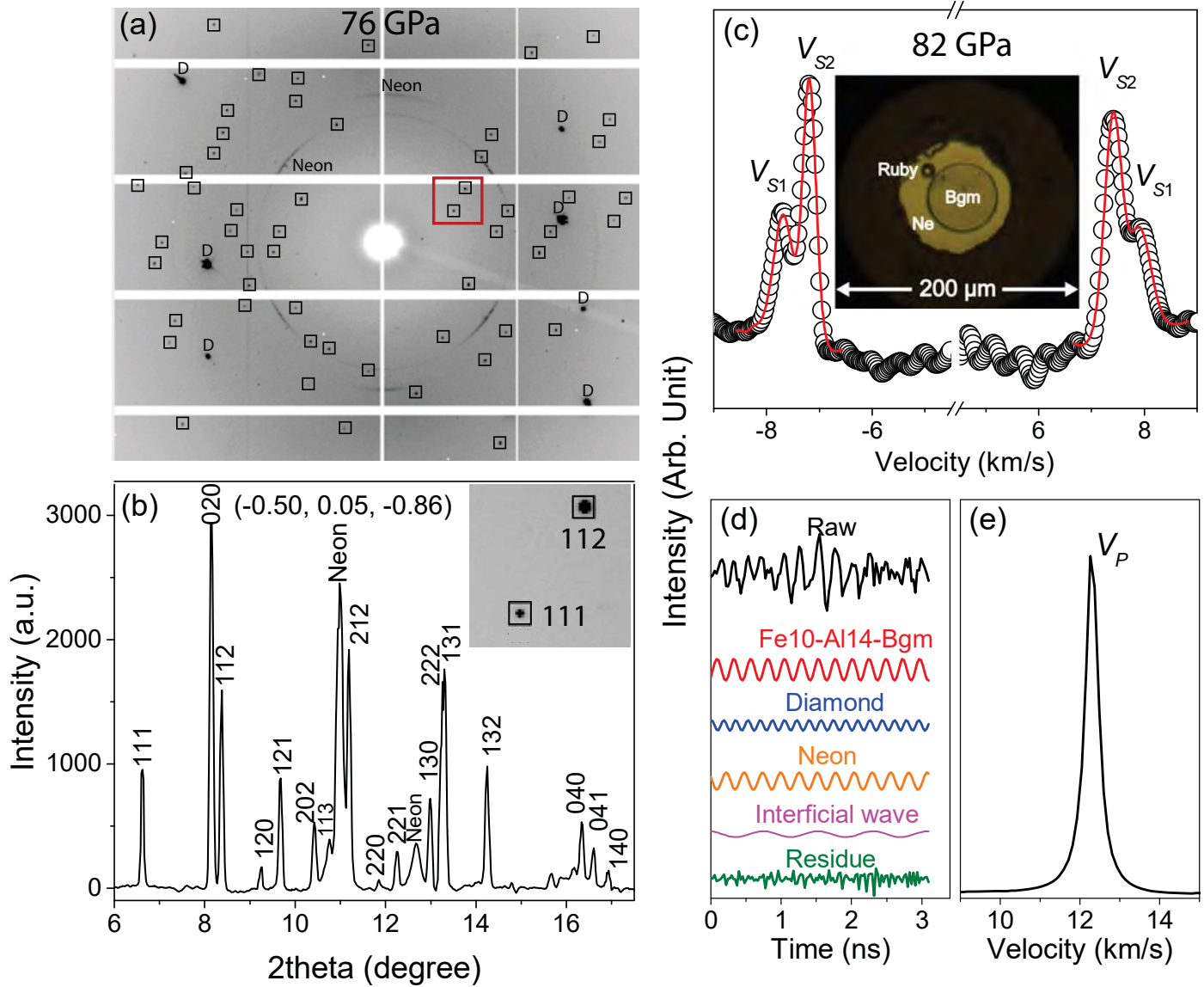


Figure 3

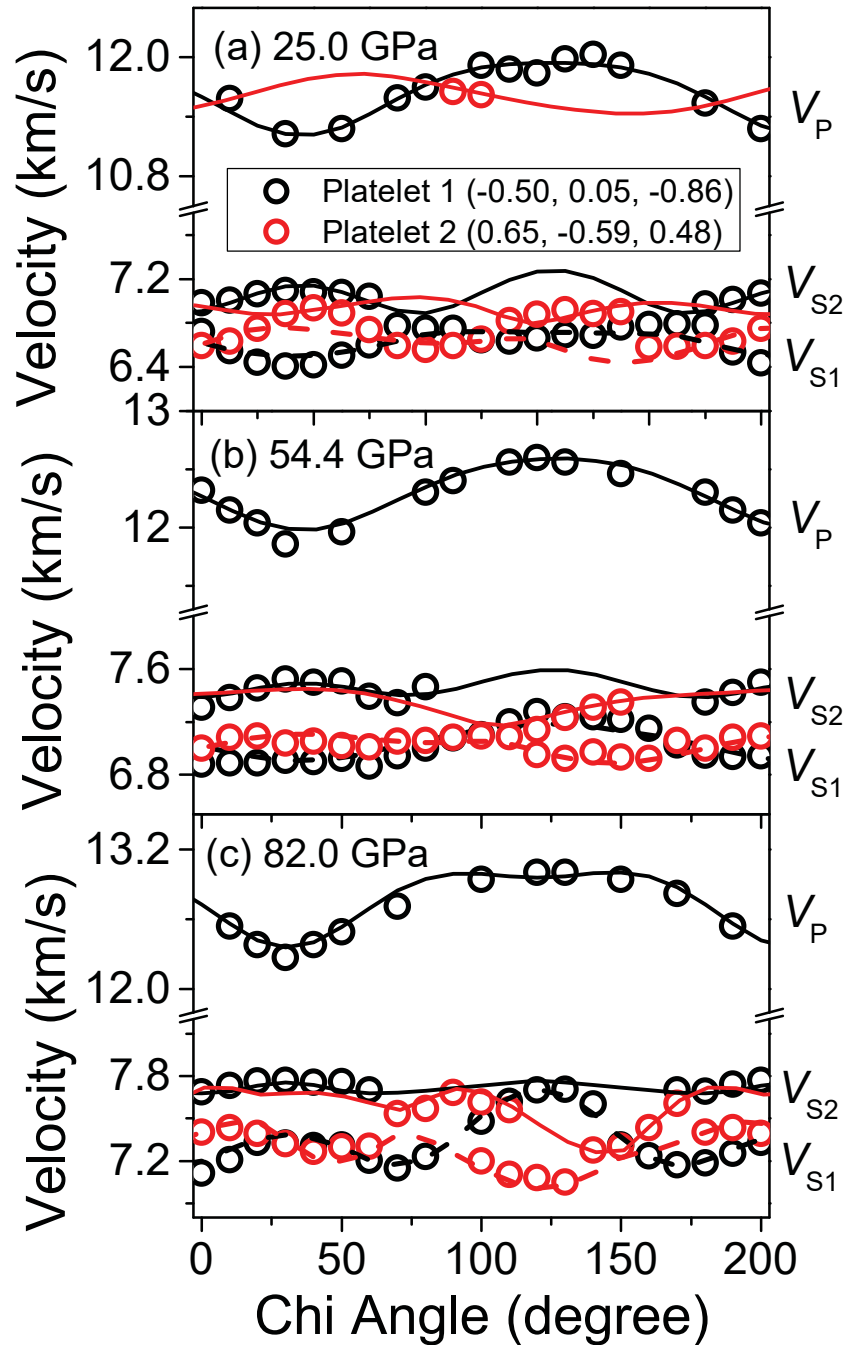


Figure 4

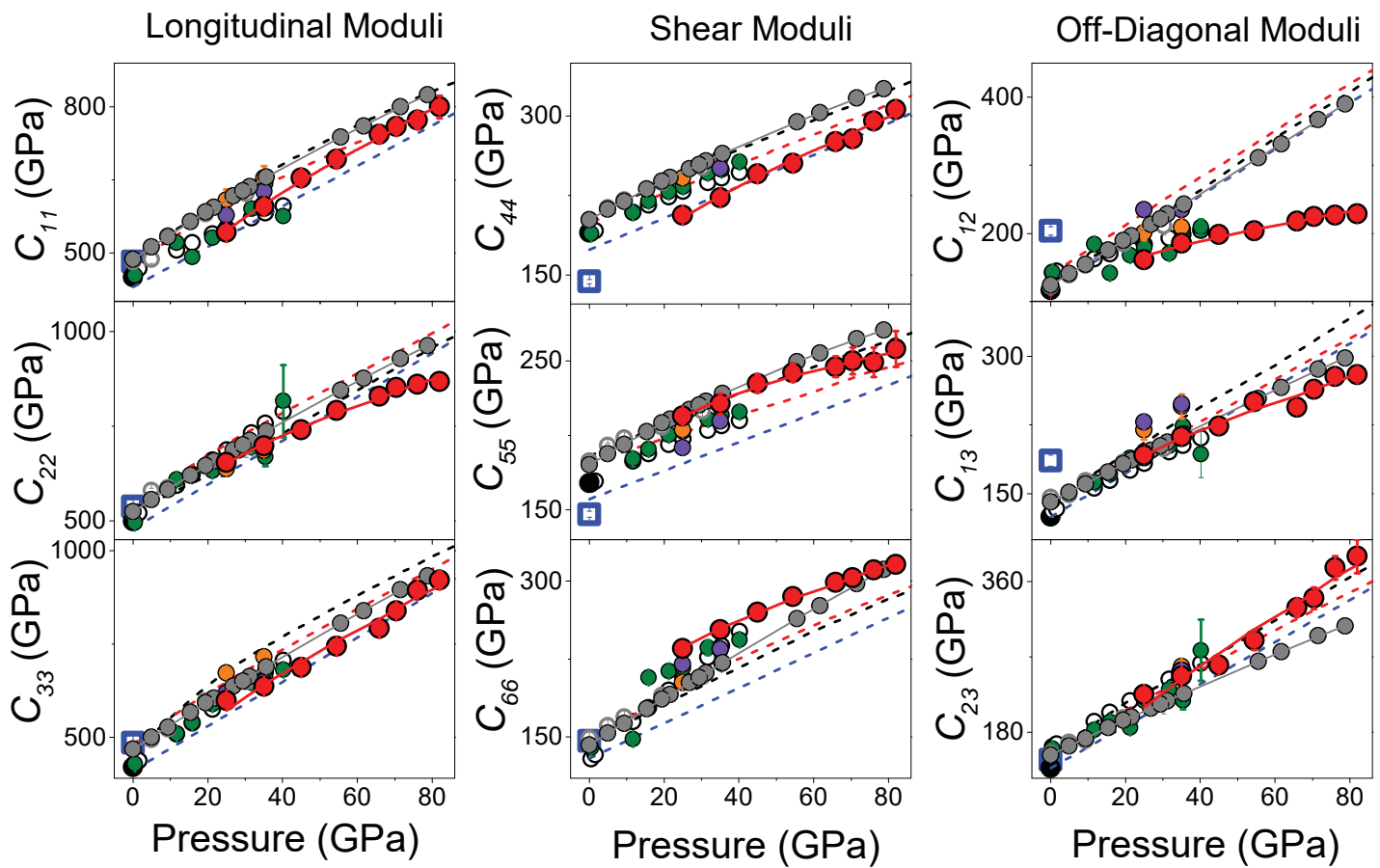


Figure 5

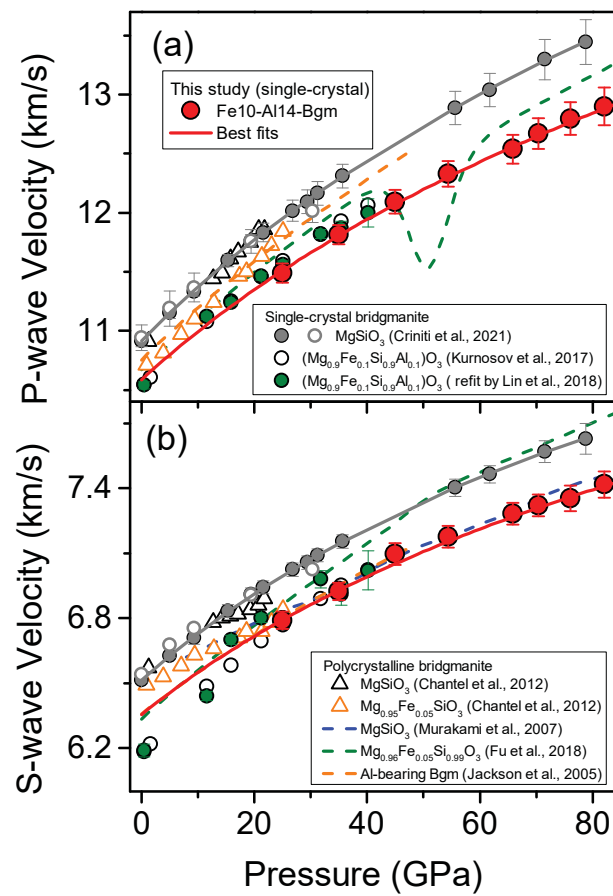


Figure 6

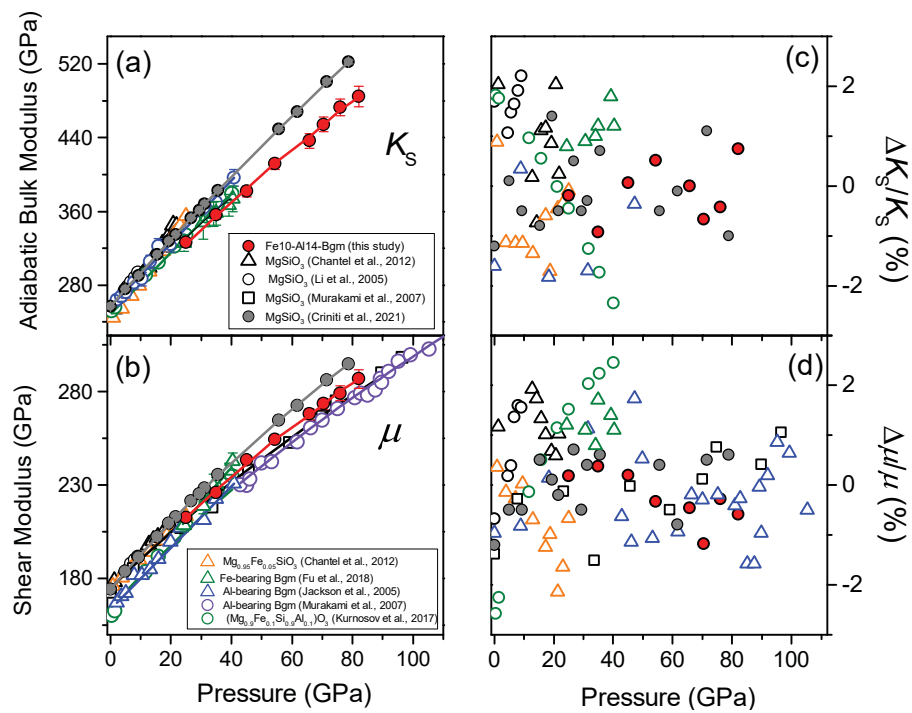


Figure 7

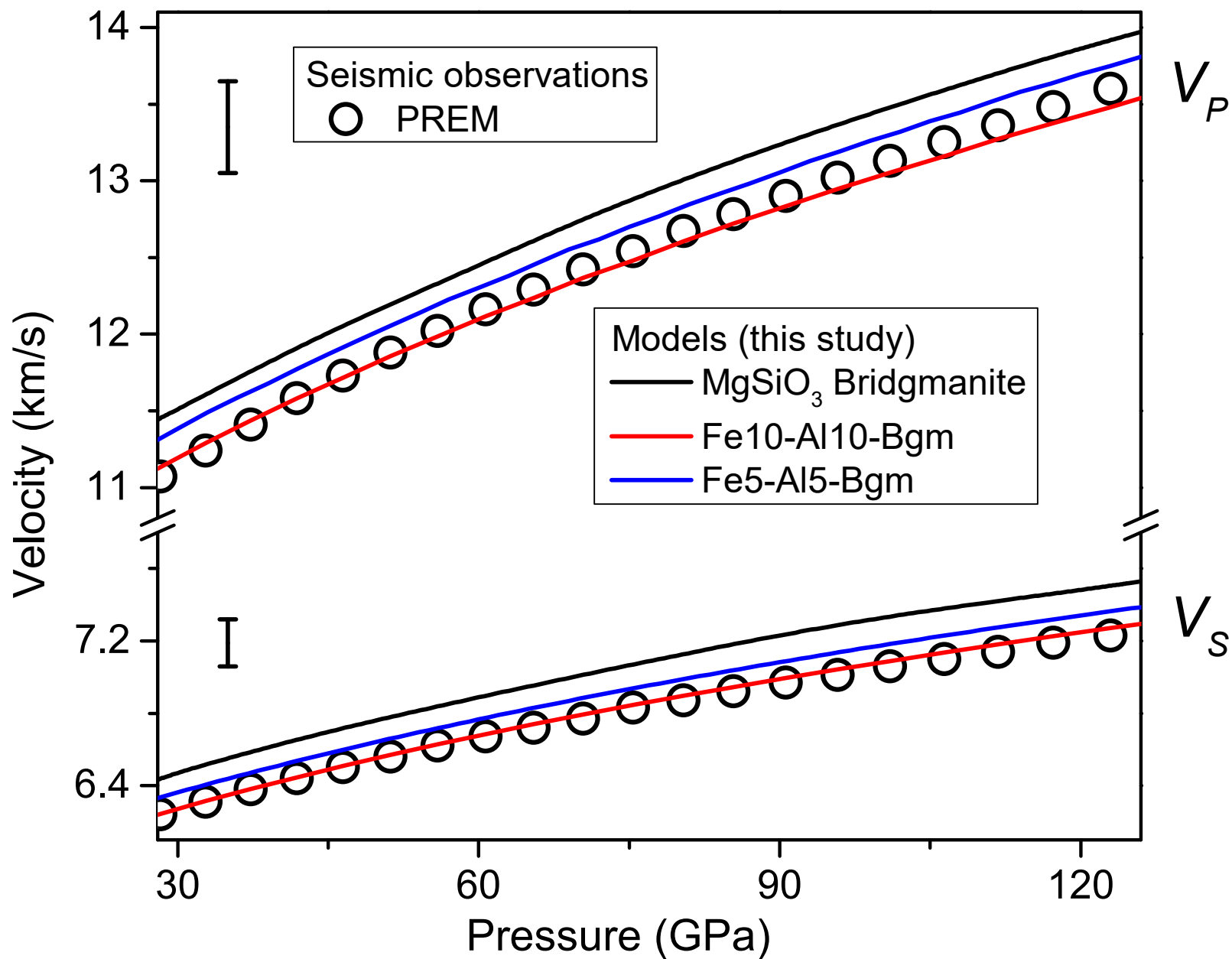


Figure 8

